

Higher-order Fabry-Pérot Interferometer from Topological Hinge States

Chang-An Li,^{1,*} Song-Bo Zhang,^{1,†} Jian Li,^{2,3} and Björn Trauzettel¹

¹*Institute for Theoretical Physics and Astrophysics,
University of Würzburg, 97074 Würzburg, Germany*

²*School of Science, Westlake University, 18 Shilongshan Road, Hangzhou 310024, Zhejiang Province, China*

³*Institute of Natural Sciences, Westlake Institute for Advanced Study,
18 Shilongshan Road, Hangzhou 310024, Zhejiang Province, China*

(Dated: February 2, 2022)

We propose an intrinsic 3D Fabry-Pérot type interferometer, coined “higher-order interferometer”, that utilizes the chiral hinge states of second-order topological insulators and *cannot* be equivalently mapped to 2D space because of higher-order topology. Quantum interference patterns in the two-terminal conductance of this interferometer are controllable not only by tuning the strength but also, particularly, by rotating the direction of the magnetic field applied perpendicularly to the transport direction. Remarkably, the conductance exhibits a characteristic beating pattern with multiple frequencies with respect to field strength or direction. Our novel interferometer provides feasible and robust magneto-transport signatures to probe the particular hinge states of higher-order topological insulators.

Introduction.—Higher-order topological insulators (HOTIs) feature gapless excitations, similar to traditional (first-order) topological insulators, that are protected by bulk electronic topology but localized at open boundaries at least two dimensions lower than the insulating bulk [1–16]. For instance, 3D second-order topological insulators (SOTIs) host 1D chiral or helical states along specific hinges of the systems. In recent years, HOTIs have triggered widespread research interest, owing to their discoveries in a variety of candidate systems, promotion of our understanding of topological states of matter, and potential applications [17–39]. So far, most efforts have been put into the potential realization and electronic characterization of HOTIs. However, the transport properties of HOTIs remain largely unexplored, despite of a few works associated with superconductivity [40–42]. Indeed, for 3D SOTIs, an intriguing open question is whether the emergent hinge states can exhibit any particular phenomena in normal-state transport.

One appealing route towards this question involves interferometers built of SOTIs, which enable us to study quantum-coherent transport of hinge states. Propagating hinge states that form interference loops enclosing a magnetic flux applied to the system pick up an Aharonov-Bohm (AB) phase [43]. In presence of quantum coherence, the AB phase will give rise to quantum oscillations in transport characteristics such as the charge conductance. Quantum interference patterns in the two-terminal conductance have been employed to detect topological phases of matter, for instance, surface states of topological insulators [44–47], chiral Majorana modes [48–51], and topological Dirac semimetals [52].

In this work, we propose a higher-order Fabry-Pérot interferometer to probe hinge states of SOTIs. Our basic setup, shown in Fig. 1(a), is composed of a rectangular chiral SOTI in contact with two leads. The chiral hinge

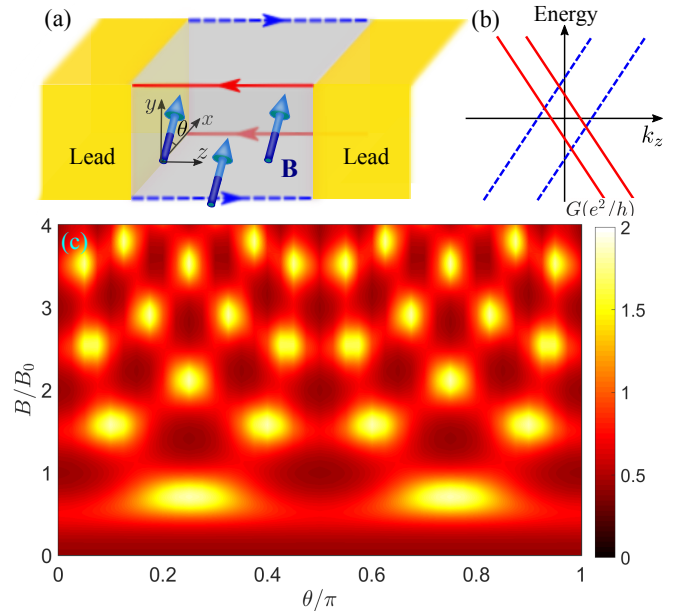


Figure 1. (a) Schematic of the higher-order interferometer: a SOTI with four chiral hinge states (solid red and dashed blue lines) are connected to two leads (yellow). Adjacent chiral hinge states form interference loops in the presence of finite reflections at the interfaces. A magnetic field \mathbf{B} perpendicular to z -direction is applied to the SOTI (gray). (b) The hinge states have linear dispersion and are shifted in k_z -direction by \mathbf{B} . (c) Density plot of conductance with respect to the field strength B and direction θ . $B_0 = \phi_0/S_f$ with ϕ_0 the flux quantum and S_f the area of the front surface of the SOTI.

states, existing in 3D space, form interference loops due to finite reflections (not shown) at the two interfaces, and their energy dispersions split in a non-uniform manner under magnetic fields, as shown in Fig. 1(b). Particular quantum interference patterns in the two-terminal conductance, arising from the AB effect as exemplified by Fig. 1(c), can be observed either by tuning the field

strength B or direction θ . In addition, owing to the intrinsic 3D nature of the interferometer, there are generally two frequencies in the magneto-conductance oscillations, leading to a beating pattern. These features do not depend on the details of the junction, such as the electronic spectrum of the leads, and are stable against disorder and dephasing. Hence, they provide robust transport signatures of hinge states in 3D SOTIs.

General analysis based on scattering matrix theory.—Our proposed interferometer involves a 3D SOTI with four chiral hinge states attached to two leads in z -direction, as sketched in Fig. 1(a). Adjacent chiral hinge states form interference loops because of finite reflections at the interfaces, as will be discussed below. A magnetic field $\mathbf{B} = B(\cos \theta, \sin \theta, 0)$ in x - y plane is applied in the SOTI region, where B measures the field strength and θ the field direction with respect to x -direction.

Before presenting concrete results based on specific models, it is instructive to analyze the main transport features of the interferometer using a phenomenological scattering matrix approach [53–55]. The transport properties of the setup are encoded in a scattering matrix that directly connects the conducting channels in the left and right leads. The scattering processes at the two interfaces between the leads and the SOTI can be described by two scattering matrices, respectively. Each matrix consists of four components: transmission from left to right $t_{L/R}$, transmission from right to left $t'_{L/R}$, reflection from the right $r_{L/R}$ and reflection from the left $r'_{L/R}$, where the subscript (L and R) distinguishes the left and right surfaces. At low energies, the only conducting channels in the SOTI are the four hinge states which have linear dispersion and are localized at the four different hinges of the cuboid. In the presence of a magnetic field, their propagation in the SOTI will pick up AB phases that can be described by a phase matrix $U \equiv e^{2i\lambda} e^{i\varphi\sigma_z \otimes \sigma_0/2} e^{i\phi\sigma_z \otimes \sigma_z/2}$, where σ_z is a Pauli matrix, σ_0 the 2×2 identity matrix,

$$\varphi = BLW_x \cos \theta \text{ and } \phi = BLW_y \sin \theta \quad (1)$$

are the magnetic fluxes threading the two surfaces, respectively, with L the distance between the two leads and $W_{x/y}$ the widths of the sample in x/y -directions. Moreover, $\lambda = k_F L$ is the dynamical phase with k_F the Fermi wave number in the absence of magnetic fields. By eliminating the scattering amplitudes in the SOTI region, we derive analytically an effective 2×2 scattering matrix that directly connects the two interfaces [56]

$$\mathcal{S}(B, \theta) = \Phi_+ (e^{-i\lambda} - e^{i\lambda} r_{L'} \Phi_- r_R \Phi_+)^{-1}, \quad (2)$$

where the phase matrices $\Phi_{\pm} \equiv e^{i(\varphi \pm \phi)\sigma_z/2}$ account for the AB phase differences between the two right-moving and between the two left-moving hinge channels, respectively. At zero temperature, the two-terminal conduc-

tance of the setup can be evaluated as

$$G(B, \theta) = \frac{e^2}{h} \text{Tr}[t_R^\dagger t_R \mathcal{S}(B, \theta) t_L t_L^\dagger \mathcal{S}^\dagger(B, \theta)], \quad (3)$$

where h is the Planck constant and e is electron charge. According to Eqs. (2) and (3), if there is no transmission across any of the two interfaces, i.e., $t_L = 0$ or $t_R = 0$, then G vanishes. In the opposite limit, where the interfaces are completely transparent for the hinge states, $r_{L'} = 0$ and $r_R = 0$, we find that the matrix \mathcal{S} as well as $t_R^\dagger t_R$ and $t_L t_L^\dagger$ become diagonal. As a result, G becomes quantized at $2e^2/h$ and is independent of the magnetic field. These results indicate the necessary condition for a successful interferometer: non-trivial transmission and reflection at the two interfaces for the hinge states.

When the interfaces are partially transparent, Eq. (2) indicates the formation of Fabry-Pérot interference loops. Moreover, the matrix \mathcal{S} contains explicitly two phases $\varphi \pm \phi$ in general. This indicates the appearance of beating patterns with two frequencies in the magneto-conductance. Notably, the two frequencies are intimately connected to the magnetic fluxes threading the different surfaces of the SOTI. They are solely determined by the geometry of the sample and insensitive to the details of the interface barriers. The oscillation pattern of G remains qualitatively the same even in the presence of a dynamic phase. We verified these results by properly parametrizing the scattering matrices [56].

Model simulation and method.—To demonstrate these features of the interferometer explicitly, we consider an effective model for chiral SOTIs [7]

$$H(\mathbf{k}) = \left(m + b \sum_{i=x,y,z} \cos k_i \right) \tau_3 + v \sum_{i=x,y,z} \sin k_i \sigma_i \tau_1 + \Delta (\cos k_x - \cos k_y) \tau_2, \quad (4)$$

where $\mathbf{k} = (k_x, k_y, k_z)$ is the wave vector. $\boldsymbol{\tau} = (\tau_1, \tau_2, \tau_3)$ and $\boldsymbol{\sigma} = (\sigma_x, \sigma_y, \sigma_z)$ are Pauli matrices acting on orbital and spin spaces, respectively; m , b , v and Δ are model parameters. Without loss of generality, we set the lattice constant and the velocity v to unity hereafter. When $1 < |m/b| < 3$ and $\Delta = 0$, the model describes 3D topological insulators with gapless surface states [57]. The surface states are protected by time-reversal symmetry $\mathcal{T} = i\sigma_2 \mathcal{K}$, where \mathcal{K} represents complex conjugation. A finite $\Delta \neq 0$ breaks time-reversal and \mathcal{C}_4 rotation (with the rotation axis pointing in z -direction) symmetries individually. It opens gaps in the surface states. However, the Δ term preserves the combined symmetry $\mathcal{C}_4 \mathcal{T}$, as indicated by $(\mathcal{C}_4 \mathcal{T}) H(k_x, k_y, k_z) (\mathcal{C}_4 \mathcal{T})^{-1} = H(k_y, -k_x, -k_z)$. As a result, the gaps opened by Δ depend on the surface orientation, leading to gapless chiral hinge states localized at the hinges connecting different surfaces.

We take into account the orbital effect of the magnetic field via the Peierls replacement in the hopping interaction $T_{ij} \rightarrow T_{ij} \exp(2\pi i \int_{r_i}^{r_j} \mathbf{dr} \cdot \mathbf{A}/\phi_0)$, where T_{ij} is the

hopping amplitude from sites r_i to r_j , $\phi_0 = h/e$ is flux quantum. \mathbf{A} is the vector potential for the magnetic field and it is chosen as $\mathbf{A} = B(0, 0, y \cos \theta - x \sin \theta)$ for concreteness [58].

For simplicity, we model the metallic leads with a conventional quadratic energy dispersion and assume only a few transport channels in both leads such that considerable reflections for the hinge channels are generated at the interfaces. Furthermore, we consider the size of the system to be much larger than the decay length of the hinge states in order to have a well-defined multiple-loop interferometer based on hinge states. Under these considerations, we calculate the two-terminal conductance numerically, employing the standard Landauer-Büttiker approach [59–61] in combination with lattice Green functions (see the Supplemental Material [56]). We emphasize that our main results illustrated below remain qualitatively the same if we choose other models for SOTIs or leads.

Quantum interference pattern.—Now, we analyze the dependence of the conductance G on the magnetic field, combining general scattering theory and concrete numerical simulations. Equation (3) implies an oscillation pattern of G with respect to the field direction θ . As shown in Fig. 2(a), $G(\theta)$ is periodic in θ , in accordance with the scattering theory. Explicitly, we find that for weak magnetic fields $B \leq B_0$, $G(\theta)$ is approximately a sinusoidal function of θ and takes the maximal value at $\theta = \pi/4 + n\pi/2$, $n \in \{0, 1, 2, 3\}$, when $W_x = W_y$. Here, B_0 corresponds to the field strength at which the flux enclosed by the front surface S_f is one flux quantum for $\theta = 0$. Thus, $G(\theta)$ has a period of $\pi/2$ in θ . Moreover, $G(\theta)$ is minimal at $\theta = \theta_c$ and symmetric in $\theta - \theta_c$, where $\theta_c = n\pi/2$. For strong magnetic fields $B > B_0$, the number of conductance peaks increases with increasing B , see Fig. 1(c). When $W_x \neq W_y$, the period in θ becomes π but $G(\theta)$ is still symmetric in $\theta - \theta_c$.

Equation (3) also indicates an oscillation pattern of G with respect to the field strength B , which is again fully confirmed by our numerical simulations. When the magnetic field is applied in x - or y -directions, or at the specific angle $\theta = \pm \arctan(W_x/W_y)$, $G(B)$ exhibits simple oscillations with a single frequency, see Fig. 2(b). Generally, the oscillating conductance takes maximal or minimal values when the interference loop encloses half a flux quantum. In our cases, $G(B)$ takes maximal values at odd multiples of $B_0/2$ for $\theta = 0$. The oscillation amplitude is relatively smaller since only two of the four loops enclose half a flux quantum at this field direction. For $\theta = \pi/4$, $G(B)$ takes maximal values at odd multiples of $B_0/\sqrt{2}$, where the interference loop also encloses half a flux quantum, leading to a resonance peak of $G(B)$. These features signify the interferometer formed by hinge states being of Fabry-Pérot type, as we further explain below.

Notably, there exist beating patterns, as signified by

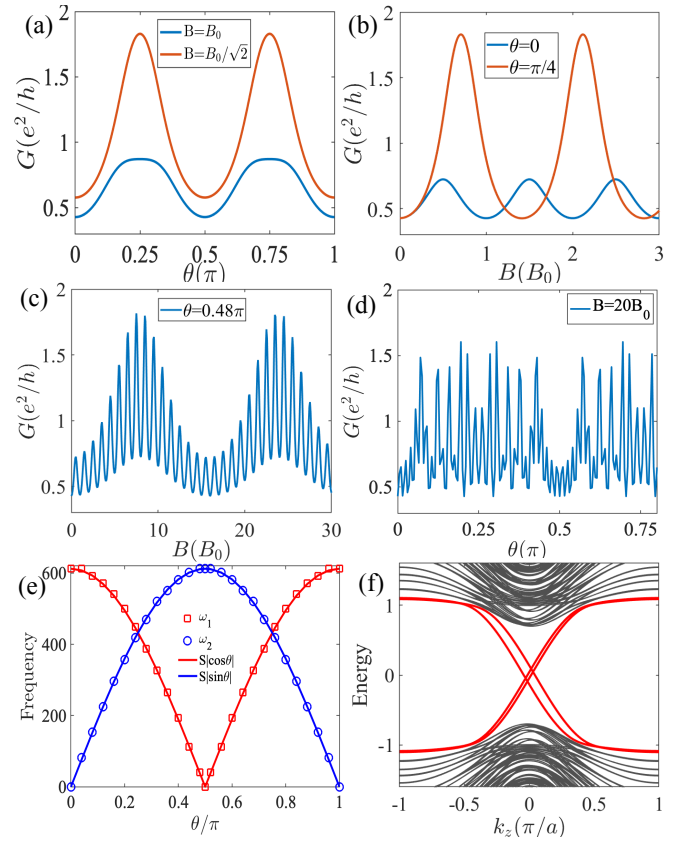


Figure 2. (a) Conductance G as a function of field direction θ at small field strengths $B = B_0$ and $B_0/\sqrt{2}$, respectively. (b) G as a function of B for $\theta = 0$ and $\pi/4$, respectively. In these cases, the oscillations have a single frequency. (c) Particular beating patterns as varying B at angle $\theta = 0.48\pi$. (d) “Irregular” beating patterns as varying θ at a large field strength $B = 20B_0$. (e) The extracted frequencies (square and circle dots) as a function of θ . The two frequencies can be described by $\omega_1 = S|\cos \theta|$ and $\omega_2 = S|\sin \theta|$. (f) The low-energy spectrum of the SOTI in the presence of a magnetic field $B = 2B_0$ and $\theta = 0.15\pi$. Other parameters are $L_z = 60a$, $W_x = W_y = 12a$, $m = 2$, $b = -1$, $v = 1$, $\Delta = 1$, and the Fermi energy $E_F = 0.002$.

Eq. (2), where the matrix \mathcal{S} explicitly contains the two phases $\varphi \pm \phi$. When the magnetic field deviates away from the special directions at $\theta = n\pi/2$ (with $n \in \{0, 1, 2, 3\}$) and $\pm \arctan(W_x/W_y)$, beating oscillations of $G(B)$ are clearly observed, as shown in Fig. 2(c). By performing discrete Fourier transformation to the beating patterns, we obtain precisely two frequencies ω_1 and ω_2 . These frequencies depend strongly on the field direction θ [dotted lines in Fig. 2(e)]. Explicitly, we find that the two frequencies can be well described by $\omega_1 = |S \cos \theta| = |\phi|/B$ and $\omega_2 = |S \sin \theta| = |\varphi|/B$ [solid lines in Fig. 2(e)], respectively, where S is the area of the surfaces of the system (we consider the case with $W_x = W_y$ for simplicity). This corresponds exactly to the two AB phases in Eq. (1), in excellent agreement with the results obtained from

scattering-matrix analysis. When $\theta = n\pi/2$, only one of the two frequencies survives. When $\theta = \pi/4 + n\pi/2$, the two frequencies become identical. In both cases, the beating behavior in the oscillations disappear. Similarly, $G(\theta)$ also shows beating-like patterns with respect to the field direction θ with irregular peaks and dips for large magnetic fields $B \gg B_0$, as shown in Fig. 2(d). This direction-induced beating behavior is another manifestation of the two AB phases.

Higher-order Fabry-Pérot interference.—Next, we clarify, in which sense our quantum interference pattern is a higher-order Fabry-Pérot type interference. The two frequencies in the beating patterns correspond physically to two areas of interference loops. As rotating the magnetic field, the two frequencies match the effective areas of front surface $|S \cos \theta|$ and top surface $|S \sin \theta|$ quite well, see Fig. 2(e). This fact indicates: (i) the adjacent hinge states with opposite chirality form effective interference loops and the interference is typically of Fabry-Pérot type; and (ii) there are totally four interference loops but any two opposite surfaces of the sample (namely, the front and back surfaces, or the top and bottom surfaces) have the same effective area because of the chosen symmetry of the system [62]. The interference loops are made of chiral hinge modes located in 3D space, protected by higher-order topology. When rotating the magnetic field, one of the frequencies increases, whereas the other one decreases. Moreover, the ratio between the two frequencies depends on θ as $S_f/S_t = W_y |\cot \theta|/W_x$. Thus, the two frequencies coincide at the critical field directions $\theta_c = \arctan(W_y/W_x)$ and $\pi - \arctan(W_y/W_x)$, as shown in Fig. 2(e). These features indicate the 3D nature of the interferometer.

The mechanism of the interferometer can be better understood by analyzing the splitting of hinge states under magnetic fields. In the absence of magnetic fields, the four chiral hinge states have a double degenerate linear spectrum in k_z -direction, i.e., $\pm v k_z$. The magnetic field gives rise to a spatially varying vector potential. Note that the hinge states are localized at different hinges of the system. The local vector potential splits the linear spectrum of the hinge states. Under the chosen gauge, the spectra of hinge states are split as $+v(k_z \pm \delta k_1^z)$ and $-v(k_z \pm \delta k_2^z)$, where the splittings are determined by $\delta k_1^z = BW_x |\sin(\theta - \pi/4)|/2$ and $\delta k_2^z = BW_y |\cos(\theta + \pi/4)|/2$ [56]. Thus, the hinge states acquire finite momenta even for vanishing Fermi energy [Fig. 2(f)]. When propagating across the SOTI region, the hinge channels pick up extra phases, $\pm \delta k_{1/2}^z L_z$. Such phases turn out to be exactly the AB phases ϕ and φ , stemming from the magnetic flux enclosed by each loop. Explicitly, the flux enclosed by front surface S_f and top surface S_t of the central SOTI region in Fig. 1(a) are given by $(\delta k_1^z + \delta k_2^z)L_z$ and $2\delta k_1^z L_z$, respectively. Plugging $\phi, \varphi = \delta k^z L_z$ into Eq. (2), this indicates that the dependence of G on \mathbf{B} can be attributed to the higher-

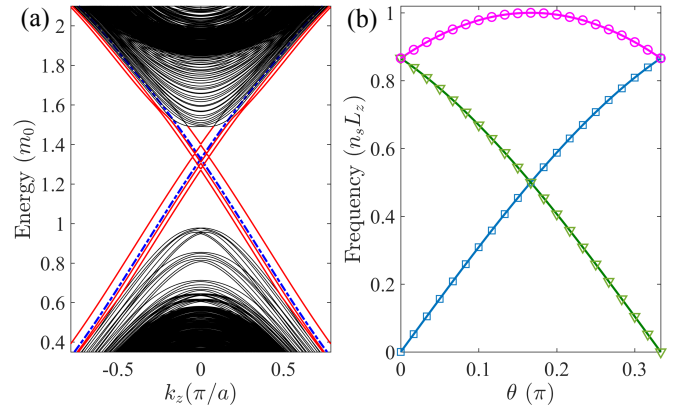


Figure 3. (a) Low-energy spectrum of the SOTI in the presence of a magnetic field. (b) The three frequencies in the case of C_6 symmetric SOTIs as functions of θ . The lattice model and related parameters can be found in the Supplemental Material [56].

order Fabry-Pérot interference of the four hinge states. At special values of θ , say $\theta = \pi/4$ or $5\pi/4$, one kind of splitting vanishes whereas the other one remains, $\delta k_1^z = 0$ and $\delta k_2^z \neq 0$ (similar results occur for $\theta = +3\pi/4, -\pi/4$). In these cases, we have only one frequency.

Generalization to C_6 symmetric SOTIs.—So far, we have focused on the case of chiral SOTIs with four hinge states and a sample with (effective) C_4 symmetry. However, our scattering theory can be generalized and applied to SOTIs with more pairs of hinge states. As an example, we consider a C_6 symmetric SOTI with three pairs of chiral hinge states [63] and show the spectrum in Fig. 3(a). The geometry considered here is a hexagonal prism with C_6 symmetry in x - y plane. The hinge states split generally with different amounts of momenta under a magnetic field. If we consider an interferometer similar to the setup in Fig. 1(a), we can also observe characteristic oscillations and beating patterns in the conductance which depend sensitively on the field direction θ . In this case, the conductance $G(\theta)$ is $\pi/3$ periodic in θ . Since there are three pairs of counter-propagating hinge states, the oscillations can exhibit three frequencies in general [56]. Figure 3(b) illustrates the three frequencies as a function of field direction θ . Particularly, the oscillations are described by a single and two frequencies for $\theta = 0$ and $\theta = \pi/6$, respectively.

Discussion and summary.—In realistic samples, disorder and dephasing [64] due to environmental noises may be detrimental to the interference pattern of hinge states. However, we show numerically that the oscillation patterns of the conductance in our setups persist under weak disorder and dephasing [56]. This indicates the robustness of our proposal. Our results based on chiral SOTIs can also be applied to helical SOTIs, which can be regarded as two copies of chiral SOTIs related by time-reversal symmetry. Recently, SOTIs have been proposed

in many candidate materials. Among these candidates, bismuth [17] and axion insulators including EuIn_2As_2 and MnBi_2Te_4 [65, 66] provide potential platforms to test our predictions.

In summary, we have proposed a higher-order Fabry-Pérot interferometer and revealed unique Aharonov-Bohm oscillations arising from topological hinge states by tuning either strength or direction of an applied magnetic field. Due to higher-order topology, the interferometer is intrinsically three-dimensional and features particular beating patterns in the magneto-conductance. Our results are robust and provide unique transport signatures of hinge states in higher-order topological insulators.

This work was supported by the DFG (SPP1666 and SFB1170 “ToCoTronics”), the Würzburg-Dresden Cluster of Excellence *ct.qmat*, EXC2147, project-id 390858490, and the Elitenetzwerk Bayern Graduate School on “Topological Insulators”. JL acknowledges support by NSFC under Grants No. 11774317.

* changan.li@uni-wuerzburg.de

† song-bo.zhang@uni-wuerzburg.de

- [1] W. A. Benalcazar, B. A. Bernevig, and T. L. Hughes, “Quantized electric multipole insulators”, *Science* **357**, 61 (2017).
- [2] W. A. Benalcazar, B. A. Bernevig, and T. L. Hughes, “Electric multipole moments, topological multipole moment pumping, and chiral hinge states in crystalline insulators”, *Phys. Rev. B* **96**, 245115 (2017).
- [3] R.-J. Slager, L. Rademaker, J. Zaanen, and L. Balents, “Impurity-bound states and Green’s function zeros as local signatures of topology”, *Phys. Rev. B* **92**, 085126 (2015).
- [4] Y. Peng, Y. Bao, and F. von Oppen, “Boundary green functions of topological insulators and superconductors”, *Phys. Rev. B* **95**, 235143 (2017).
- [5] J. Langbehn, Y. Peng, L. Trifunovic, F. von Oppen, and P. W. Brouwer, “Reflection-symmetric second-order topological insulators and superconductors”, *Phys. Rev. Lett.* **119**, 246401 (2017).
- [6] Z. Song, Z. Fang, and C. Fang, “ $(d-2)$ -dimensional edge states of rotation symmetry protected topological states”, *Phys. Rev. Lett.* **119**, 246402 (2017).
- [7] F. Schindler, A. M. Cook, M. G. Vergniory, Z. Wang, S. S. P. Parkin, B. A. Bernevig, and T. Neupert, “Higher-order topological insulators”, *Science Advances* **4** (2018).
- [8] M. Geier, L. Trifunovic, M. Hoskam, and P. W. Brouwer, “Second-order topological insulators and superconductors with an order-two crystalline symmetry”, *Phys. Rev. B* **97**, 205135 (2018).
- [9] M. Ezawa, “Higher-order topological insulators and semimetals on the breathing kagome and pyrochlore lattices”, *Phys. Rev. Lett.* **120**, 026801 (2018).
- [10] E. Khalaf, “Higher-order topological insulators and superconductors protected by inversion symmetry”, *Phys. Rev. B* **97**, 205136 (2018).
- [11] M. J. Park, Y. Kim, G. Y. Cho, and S. Lee, “Higher-order topological insulator in twisted bilayer graphene”, *Phys. Rev. Lett.* **123**, 216803 (2019).
- [12] L. Trifunovic and P. W. Brouwer, “Higher-order bulk-boundary correspondence for topological crystalline phases”, *Phys. Rev. X* **9**, 011012 (2019).
- [13] Y. You, T. Devakul, F. J. Burnell, and T. Neupert, “Higher-order symmetry-protected topological states for interacting bosons and fermions”, *Phys. Rev. B* **98**, 235102 (2018).
- [14] T. Hirose, S. A. Díaz, J. Klinovaja, and D. Loss, “Magnonic quadrupole topological insulator in antiskyrmion crystals”, *Phys. Rev. Lett.* **125**, 207204 (2020).
- [15] S. Franca, J. van den Brink, and I. C. Fulga, “An anomalous higher-order topological insulator”, *Phys. Rev. B* **98**, 201114 (2018).
- [16] G. van Miert and C. Ortix, “Higher-order topological insulators protected by inversion and rotoinversion symmetries”, *Phys. Rev. B* **98**, 081110 (2018).
- [17] F. Schindler, Z. Wang, M. G. Vergniory, A. M. Cook, A. Murani, S. Sengupta, *et al.*, “Higher-order topology in bismuth”, *Nat. Phys.* **14**, 918 (2018).
- [18] S. Imhof, C. Berger, F. Bayer, J. Brehm, L. W. Molenkamp, T. Kiessling, *et al.*, “Topoelectrical-circuit realization of topological corner modes”, *Nat. Phys.* **14**, 925 (2018).
- [19] C. W. Peterson, W. A. Benalcazar, T. L. Hughes, and G. Bahl, “A quantized microwave quadrupole insulator with topologically protected corner states”, *Nature* **555**, 346 (2018).
- [20] M. Serra-Garcia, V. Peri, R. Süsstrunk, O. R. Bilal, T. Larsen, L. G. Villanueva, and S. D. Huber, “Observation of a phononic quadrupole topological insulator”, *Nature* **555**, 342 (2018).
- [21] X.-D. Chen, W.-M. Deng, F.-L. Shi, F.-L. Zhao, M. Chen, and J.-W. Dong, “Direct observation of corner states in second-order topological photonic crystal slabs”, *Phys. Rev. Lett.* **122**, 233902 (2019).
- [22] Y. Peng and G. Refael, “Floquet Second-Order Topological Insulators from Nonsymmorphic Space-Time Symmetries”, *Phys. Rev. Lett.* **123**, 016806 (2019).
- [23] A. K. Ghosh, G. C. Paul, and A. Saha, “Higher order topological insulator via periodic driving”, *Phys. Rev. B* **101**, 235403 (2020).
- [24] A. El Hassan, F. K. Kunst, A. Moritz, G. Andler, E. J. Bergholtz, and M. Bourennane, “Corner states of light in photonic waveguides”, *Nat. Photonics* **13**, 697 (2019).
- [25] X. Ni, M. Weiner, A. Alù, and A. B. Khanikaev, “Observation of higher-order topological acoustic states protected by generalized chiral symmetry”, *Nat. Mater.* **18**, 113 (2019).
- [26] B.-Y. Xie, G.-X. Su, H.-F. Wang, H. Su, X.-P. Shen, P. Zhan, M.-H. Lu, Z.-L. Wang, and Y.-F. Chen, “Visualization of higher-order topological insulating phases in two-dimensional dielectric photonic crystals”, *Phys. Rev. Lett.* **122**, 233903 (2019).
- [27] Y. Qi, C. Qiu, M. Xiao, H. He, M. Ke, and Z. Liu, “Acoustic realization of quadrupole topological insulators”, *Phys. Rev. Lett.* **124**, 206601 (2020).
- [28] D. Călugăru, V. Juričić, and B. Roy, “Higher-order topological phases: A general principle of construction”, *Phys. Rev. B* **99**, 041301 (2019).
- [29] A. L. Szabó, R. Moessner, and B. Roy, “Strain-engineered higher-order topological phases for spin- $\frac{3}{2}$ Luttinger fermions”, *Phys. Rev. B* **101**, 121301 (2020).
- [30] X.-L. Sheng, C. Chen, H. Liu, Z. Chen, Z.-M. Yu, Y. X.

- Zhao, and S. A. Yang, “Two-dimensional second-order topological insulator in graphdiyne”, *Phys. Rev. Lett.* **123**, 256402 (2019).
- [31] C.-A. Li and S.-S. Wu, “Topological states in generalized electric quadrupole insulators”, *Phys. Rev. B* **101**, 195309 (2020).
- [32] C.-A. Li, B. Fu, Z.-A. Hu, J. Li, and S.-Q. Shen, “Topological phase transitions in disordered electric quadrupole insulators”, *Phys. Rev. Lett.* **125**, 166801 (2020).
- [33] H. Li and K. Sun, “Pfaffian formalism for higher-order topological insulators”, *Phys. Rev. Lett.* **124**, 036401 (2020).
- [34] X. Zhu, “Tunable Majorana corner states in a two-dimensional second-order topological superconductor induced by magnetic fields”, *Phys. Rev. B* **97**, 205134 (2018).
- [35] X.-W. Luo and C. Zhang, “Higher-order topological corner states induced by gain and loss”, *Phys. Rev. Lett.* **123**, 073601 (2019).
- [36] M. Ezawa, “Braiding of Majorana-like corner states in electric circuits and its non-Hermitian generalization”, *Phys. Rev. B* **100**, 045407 (2019).
- [37] S.-B. Zhang, A. Calzona, and B. Trauzettel, “All-electrically tunable networks of Majorana bound states”, *Phys. Rev. B* **102**, 100503 (2020).
- [38] S.-B. Zhang, W. B. Rui, A. Calzona, S.-J. Choi, A. P. Schnyder, and B. Trauzettel, “Topological and holographic quantum computation based on second-order topological superconductors”, *Phys. Rev. Research* **2**, 043025 (2020).
- [39] T. E. Pahlom, M. Sigrist, and A. A. Soluyanov, “Braiding Majorana corner modes in a second-order topological superconductor”, *Phys. Rev. Research* **2**, 032068 (2020).
- [40] R. Queiroz and A. Stern, “Splitting the hinge mode of higher-order topological insulators”, *Phys. Rev. Lett.* **123**, 036802 (2019).
- [41] C.-Z. Li, A.-Q. Wang, C. Li, W.-Z. Zheng, A. Brinkman, D.-P. Yu, and Z.-M. Liao, “Reducing electronic transport dimension to topological hinge states by increasing geometry size of Dirac semimetal Josephson junctions”, *Phys. Rev. Lett.* **124**, 156601 (2020).
- [42] Y.-B. Choi, Y. Xie, C.-Z. Chen, J. Park, S.-B. Song, J. Yoon, *et al.*, “Evidence of higher-order topology in multilayer WTe₂ from Josephson coupling through anisotropic hinge states”, *Nat. Mater.* **19**, 974 (2020).
- [43] Y. Aharonov and D. Bohm, “Significance of electromagnetic potentials in the quantum theory”, *Phys. Rev.* **115**, 485 (1959).
- [44] J. H. Bardarson, P. W. Brouwer, and J. E. Moore, “Aharonov-Bohm oscillations in disordered topological insulator nanowires”, *Phys. Rev. Lett.* **105**, 156803 (2010).
- [45] Y. Zhang and A. Vishwanath, “Anomalous Aharonov-Bohm conductance oscillations from topological insulator surface states”, *Phys. Rev. Lett.* **105**, 206601 (2010).
- [46] H. Peng, K. Lai, D. Kong, S. Meister, Y. Chen, X.-L. Qi, S.-C. Zhang, Z.-X. Shen, and Y. Cui, “Aharonov-Bohm interference in topological insulator nanoribbons”, *Nat. Mater.* **9**, 225 (2010).
- [47] J. H. Bardarson and J. E. Moore, “Quantum interference and Aharonov-Bohm oscillations in topological insulators”, *Rep. Prog. Phys.* **76**, 056501 (2013).
- [48] A. R. Akhmerov, J. Nilsson, and C. W. J. Beenakker, “Electrically detected interferometry of Majorana fermions in a topological insulator”, *Phys. Rev. Lett.* **102**, 216404 (2009).
- [49] L. Fu and C. L. Kane, “Probing neutral Majorana fermion edge modes with charge transport”, *Phys. Rev. Lett.* **102**, 216403 (2009).
- [50] J. Li, G. Fleury, and M. Büttiker, “Scattering theory of chiral Majorana fermion interferometry”, *Phys. Rev. B* **85**, 125440 (2012).
- [51] C.-A. Li, J. Li, and S.-Q. Shen, “Majorana-Josephson interferometer”, *Phys. Rev. B* **99**, 100504 (2019).
- [52] L.-X. Wang, C.-Z. Li, D.-P. Yu, and Z.-M. Liao, “Aharonov-Bohm oscillations in Dirac semimetal Cd₃As₂ nanowires”, *Nat. Commun.* **7**, 10769 (2016).
- [53] M. Büttiker, “Scattering theory of current and intensity noise correlations in conductors and wave guides”, *Phys. Rev. B* **46**, 12485 (1992).
- [54] Y. V. Nazarov and Y. M. Blanter, *Quantum Transport: Introduction to Nanoscience* (Cambridge University Press, 2006).
- [55] J. Maciejko, E.-A. Kim, and X.-L. Qi, “Spin Aharonov-Bohm effect and topological spin transistor”, *Phys. Rev. B* **82**, 195409 (2010).
- [56] See the Supplemental Material including Refs. [59–61, 63, 64, 67, 68] for details of (Sec. S1) the general scattering matrix analysis; (Sec. S2) chiral hinge states under magnetic fields; (Sec. S3) numerical simulations; (Sec. S4) trivial cases with perfect transmission; (Sec. S5) parameterizing the scattering matrix; (Sec. S6) the effective model for C6 symmetric SOTs; (Sec. S7) the influence of disorder and dephasing; and (Sec. S8) multiple frequencies when the cross section is a trapezoid.
- [57] H. Zhang, C. X. Liu, X. L. Qi, X. Dai, Z. Fang, and S. C. Zhang, “Topological insulators in Bi₂Se₃, Bi₂Te₃ and Sb₂Te₃ with a single Dirac cone on the surface”, *Nat. Phys.* **5**, 438 (2009).
- [58] We ignore the Zeeman interaction in this model because it is expected to have a minor influence on the AB effect.
- [59] R. Landauer, “Electrical resistance of disordered one-dimensional lattices”, *Philos. Mag.* **21**, 863 (1970).
- [60] M. Büttiker, “Four-Terminal Phase-Coherent Conductance”, *Phys. Rev. Lett.* **57**, 1761 (1986).
- [61] S. Datta, *Electronic Transport in Mesoscopic Systems* (Cambridge University Press, Cambridge, 1995).
- [62] We also consider a geometry with lower symmetry, for instance, the cross section is a trapezoid, see the Supplementary Material [56].
- [63] R.-X. Zhang, F. Wu, and S. Das Sarma, “Möbius insulator and higher-order topology in MnBi_{2n}Te_{3n+1}”, *Phys. Rev. Lett.* **124**, 136407 (2020).
- [64] H. Jiang, S. Cheng, Q.-F. Sun, and X. C. Xie, “Topological insulator: A new quantized spin hall resistance robust to dephasing”, *Phys. Rev. Lett.* **103**, 036803 (2009).
- [65] Y. Xu, Z. Song, Z. Wang, H. Weng, and X. Dai, “Higher-order topology of the axion insulator EuIn₂As₂”, *Phys. Rev. Lett.* **122**, 256402 (2019).
- [66] R. Chen, S. Li, H.-P. Sun, Y. Zhao, H.-Z. Lu, and X. C. Xie, “Using nonlocal surface transport to identify the axion insulator”, arXiv:2005.14074.
- [67] C. W. Groth, M. Wimmer, A. R. Akhmerov, and X. Waintal, “Kwant: a software package for quantum transport”, *New J. Phys.* **16**, 063065 (2014).
- [68] A. MacKinnon, “The calculation of transport properties and density of states of disordered solids”, *Z. Phys. B Condens. Matter* **59**, 385 (1985).

Supplemental material for “Higher-order Fabry-Pérot Interferometer from Topological Hinge States”

Appendix S1: General scattering matrix analysis

In this section, we present the details for the scattering matrix analysis of the setup in the main text. Suppose there are $p_{L/R}$ conducting modes at the Fermi level in the left/right leads. We can define generally $(p_{L/R} + 2) \times (p_{L/R} + 2)$ scattering matrices, S_L and S_R , to describe the scattering at the left and right interfaces, respectively,

$$\begin{pmatrix} b_L \\ b_{L'} \end{pmatrix} = S_L \begin{pmatrix} a_L \\ a_{L'} \end{pmatrix}, \quad S_L = \begin{pmatrix} r_L & t_{L'} \\ t_L & r_{L'} \end{pmatrix}, \quad (\text{S1.1})$$

$$\begin{pmatrix} b_{R'} \\ b_R \end{pmatrix} = S_R \begin{pmatrix} a_{R'} \\ a_R \end{pmatrix}, \quad S_R = \begin{pmatrix} r_R & t_{R'} \\ t_R & r_{R'} \end{pmatrix}. \quad (\text{S1.2})$$

Here, $a_{L/R}$ and $b_{L/R}$ indicate the incoming and outgoing modes that propagate in the leads and scatter at the left/right interface, respectively; $a_{L'/R'}$ and $b_{L'/R'}$ indicate the incoming and outgoing hinge modes that propagate in the SOTI and scatter at the left/right interface, respectively. The scattering matrix $S_{L/R}$ consists of four components $t_{L/R}$, $t'_{L/R}$, $r_{L/R}$, and $r'_{L/R}$, corresponding to the transmission from left to right, transmission from right to left, reflection from the right, and reflection from the left, respectively. In the center SOTI region, the conducting chiral hinge states pick up an AB phases when applying an external magnetic field. Thus, the incoming and outgoing modes in the SOTI can be connected by a phase matrix as

$$\begin{pmatrix} a_{R'1} \\ a_{R'2} \\ a_{L'1} \\ a_{L'2} \end{pmatrix} = e^{i\lambda/2} \begin{pmatrix} e^{i(\varphi+\phi)/2} & 0 & 0 & 0 \\ 0 & e^{-i(\varphi+\phi)/2} & 0 & 0 \\ 0 & 0 & e^{i(\varphi-\phi)/2} & 0 \\ 0 & 0 & 0 & e^{-i(\varphi-\phi)/2} \end{pmatrix} \begin{pmatrix} b_{L'1} \\ b_{L'2} \\ b_{R'1} \\ b_{R'2} \end{pmatrix}, \quad (\text{S1.3})$$

where $\lambda = k_F L$ is the dynamic phase with k_F the Fermi wave number in k_z -direction and L the length of the SOTI, and the two phases are given by

$$\phi = BS_1 \sin \theta, \quad \varphi = BS_2 \cos \theta, \quad (\text{S1.4})$$

with θ the angle between the magnetic field direction and x -axis.

Substituting Eq. (S1.3) into Eq. (S1.2), we obtain

$$\begin{pmatrix} e^{-i\lambda/2} \Phi_-^\dagger a_{L'} \\ b_R \end{pmatrix} = S_R \begin{pmatrix} e^{i\lambda/2} \Phi_+ b_{L'} \\ a_R \end{pmatrix}, \quad (\text{S1.5})$$

where $\Phi_\pm \equiv e^{i(\varphi \pm \phi)\sigma_z/2}$ and the Pauli matrix σ_z acts on (pseudo-)spin space for two left- or right-moving hinge states. Writing Eqs. (S1.5) explicitly, we have

$$e^{-i\lambda/2} \Phi_-^\dagger a_{L'} = e^{i\lambda/2} r_R \Phi_+ b_{L'} + t_{R'} a_R, \quad (\text{S1.6})$$

$$b_R = e^{i\lambda/2} t_R \Phi_+ b_{L'} + r_{R'} a_R. \quad (\text{S1.7})$$

From Eq. (S1.6), we find

$$a_{L'} = e^{i\lambda} \Phi_- r_R \Phi_+ b_{L'} + e^{i\lambda/2} \Phi_- t_{R'} a_R. \quad (\text{S1.8})$$

Writing Eq. (S1.1) explicitly, we have

$$b_L = r_L a_L + t_{L'} a_{L'}, \quad (\text{S1.9})$$

$$b_{L'} = t_L a_L + r_{L'} a_{L'}, \quad (\text{S1.10})$$

Plugging Eq. (S1.8) into Eq. (S1.10), we obtain

$$b_{L'} = t_L a_L + r_{L'} (e^{i\lambda} \Phi_- r_R \Phi_+ b_{L'} + e^{i\lambda/2} \Phi_- t_{R'} a_R), \quad (\text{S1.11})$$

and hence,

$$b_{L'} = (1 - e^{i\lambda} r_{L'} \Phi_- r_R \Phi_+)^{-1} (t_L a_L + e^{i\lambda/2} r_{L'} \Phi_- t_{R'} a_R). \quad (\text{S1.12})$$

Plugging this result into Eq. (S1.7), we find b_R as

$$\begin{aligned} b_R &= t_R e^{i\lambda/2} \Phi_+ (1 - e^{i\lambda} r_{L'} \Phi_- r_R \Phi_+)^{-1} (t_L a_L + e^{i\lambda/2} r_{L'} \Phi_- t_{R'} a_R) + r_{R'} a_R \\ &= e^{i\lambda/2} t_R \Phi_+ (1 - e^{i\lambda} r_{L'} \Phi_- r_R \Phi_+)^{-1} t_L a_L + [e^{i\lambda} t_R \Phi_+ (1 - e^{i\lambda} r_{L'} \Phi_- r_R \Phi_+)^{-1} r_{L'} \Phi_- t_{R'} + r_{R'}] a_R. \end{aligned} \quad (\text{S1.13})$$

Plugging Eq. (S1.10) into Eq. (S1.6), we obtain

$$e^{-i\lambda/2} \Phi_-^\dagger a_{L'} = e^{i\lambda/2} r_R \Phi_+ (t_L a_L + r_{L'} a_{L'}) + t_{R'} a_R, \quad (\text{S1.14})$$

and hence,

$$a_{L'} = (1 - e^{i\lambda} \Phi_- r_{L'})^{-1} (e^{i\lambda} \Phi_- r_R \Phi_+ t_L a_L + e^{i\lambda/2} \Phi_- t_{R'} a_R). \quad (\text{S1.15})$$

Plugging Eq. (S1.15) into Eq. (S1.9), we find b_L as

$$\begin{aligned} b_L &= r_L a_L + t_{L'} (1 - e^{i\lambda} \Phi_- r_{L'})^{-1} (e^{i\lambda} \Phi_- r_R \Phi_+ t_L a_L + e^{i\lambda/2} \Phi_- t_{R'} a_R) \\ &= [r_L + e^{i\lambda} t_{L'} (1 - e^{i\lambda} \Phi_- r_{L'})^{-1} \Phi_- r_R \Phi_+ t_L] a_L + e^{i\lambda/2} t_{L'} (1 - e^{i\lambda} \Phi_- r_{L'})^{-1} \Phi_- t_{R'} a_R. \end{aligned} \quad (\text{S1.16})$$

Rewriting Eqs. (S1.13) and (S1.16), we obtain the effective scattering matrix of the junction

$$\begin{pmatrix} b_L \\ b_R \end{pmatrix} = S \begin{pmatrix} a_L \\ a_R \end{pmatrix}, \quad S = \begin{pmatrix} r & t' \\ t & r' \end{pmatrix}, \quad (\text{S1.17})$$

where

$$\begin{aligned} t &= t_R S t_L, \quad r' = r_{R'} + e^{i\lambda/2} t_R S r_{L'} \Phi_- t_{R'}, \\ r &= r_L + e^{i\lambda/2} t_{L'} S' r_R \Phi_+ t_L, \quad t' = t_{L'} S' t_{R'}, \\ S &= e^{i\lambda/2} \Phi_+ (1 - e^{i\lambda} r_{L'} \Phi_- r_R \Phi_+)^{-1}, \\ S' &= e^{i\lambda/2} (1 - e^{i\lambda} \Phi_- r_{L'})^{-1} \Phi_-. \end{aligned} \quad (\text{S1.18})$$

With this general scattering matrix, the two-terminal conductance can be written as

$$G(B, \theta) = \frac{e^2}{h} \text{tr}(t t^\dagger) = \frac{e^2}{h} \text{tr}(t_R^\dagger t_R S t_L t_L^\dagger S^\dagger). \quad (\text{S1.19})$$

Appendix S2: Chiral hinge states under magnetic fields

In this section, we demonstrate the splitting behavior of the chiral hinge states when rotating the magnetic field. In the absence of magnetic fields, the four chiral hinge states have a double degenerate linear spectrum in k_z -direction. The left-moving hinge states cross with the right-moving ones at $k_z = 0$. The magnetic field gives rise to a spatially varying vector potential. Remember that the hinge states are localized at different hinges of the system. The local vector potential splits the linear spectrum of hinge states. Under the chosen gauge for the vector potential, $\mathbf{A} = (0, 0, B[y \cos \theta - x \sin \theta])$, the spectrum of hinge states is split as $+v(k_z \pm \delta k_1^z)$ and $-v(k_z \pm \delta k_2^z)$, where the splitting strengths are determined by $\delta k_1^z = BW_x |\sin(\theta - \pi/4)/2|$ and $\delta k_2^z = BW_y |\cos(\theta + \pi/4)/2|$. Thus, the splitting of hinge state spectrum strongly depends on the field direction θ .

We focus on the splitting of the chiral hinge states in the lower-energy spectrum presented in Fig. S1. At $\theta = 0\pi$, two pairs of the hinge states split by equal value. At $\theta = \pi/4$, only one pair of the hinge states can be split, whereas the other one remain unaltered, i.e., $\delta k_1^z = 0$. The spectrum at $\theta = \pi/2$ looks the same as for $\theta = 0$. Another special field direction is at $\theta = 3\pi/4$ at which we have instead $\delta k_2^z = 0$. At $\theta = \pi$, the spectrum is the same as that at $\theta = 0$. This evolution with rotating the magnetic field is consistent with the analytical results $\delta k_1^z = BW_x |\sin(\theta - \pi/4)/2|$ and $\delta k_2^z = BW_y |\cos(\theta + \pi/4)/2|$.

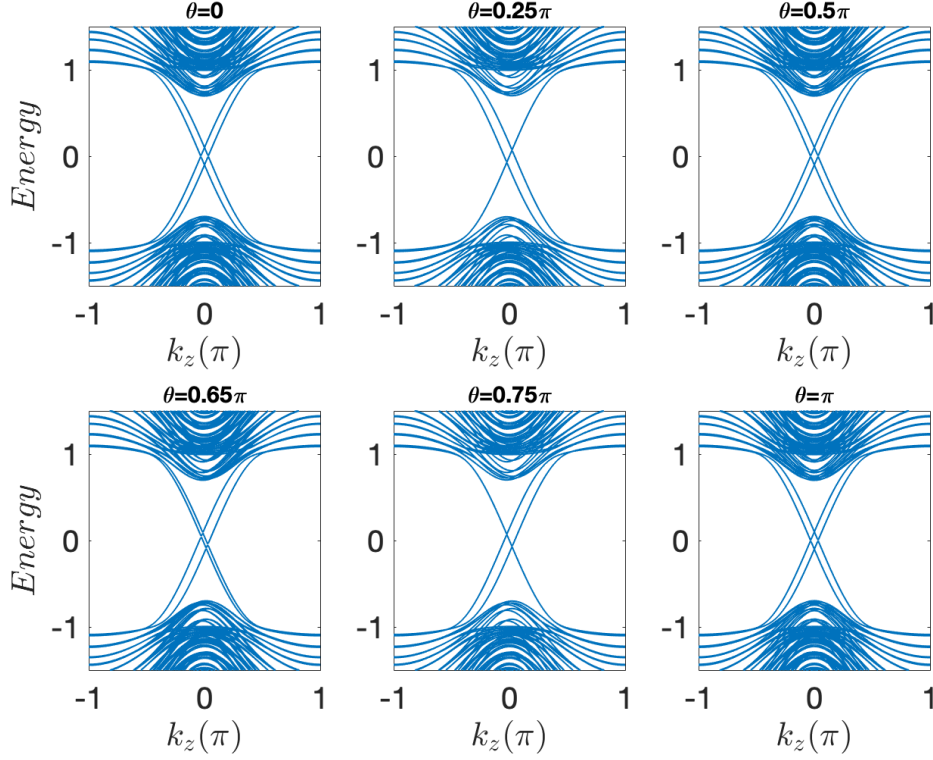


Figure S1. Evolution of the hinge states spectrum when rotating the field direction from $\theta = 0$ to π . Here, we choose parameters: $L_z = 60a$, $W_x = W_y = 12a$, $m = 2$, $b = -1$, $v = 1$, $\Delta = 1$. The field strength is fixed at $B = 2B_0$.

Appendix S3: Numerical simulation details

To calculate the conductance, we employ the Landauer-Büttiker formalism [59–61] in combination with lattice Green functions. The two-terminal conductance is evaluated as

$$G = \frac{e^2}{h} \text{Tr}[\Gamma_L G^r \Gamma_R G^a], \quad (\text{S3.1})$$

where the line width function

$$\Gamma_\beta = i[\Sigma_\beta - \Sigma_\beta^\dagger] \quad (\text{S3.2})$$

with the Σ_β being the self-energy due to coupling of the lead $\beta \in \{L, R\}$ to the central region of interest. The retarded and advanced Green function, G^r and G^a , are obtained as

$$G^r = (G^a)^\dagger = (E_F - H_c - \Sigma_L^r - \Sigma_R^r)^{-1}. \quad (\text{S3.3})$$

Here, both the self-energy Σ_β and the Green function $G^{r/a}$ can be calculated by using the recursive method [68].

In the numerical simulations, we choose the parameters $L_z = 60a$, $W_x = W_y = 12a$, $m = 2$, $b = -1$, $v = 1$ and $\Delta = 1$ for the SOHI, and $m = 3$, $v = 0$, $b = -1$, and $\Delta = 0$, and chemical potential $\mu = -0.1$ for the two leads. Without loss of generality, we set the Fermi energy in the SOHI at $E_F = 0.002$.

Appendix S4: Trivial cases of perfect transmission

In this section, we demonstrate the behaviors when the interfaces of the proposed setup are totally transparent. Under this condition, the chiral hinge states do not talk to each other and thus no interference loop is forming. As a result, the two-terminal conductance G is quantized at $2e^2/h$ and independent of the magnetic field. Let us consider two scenarios responsible for such transparent interfaces:

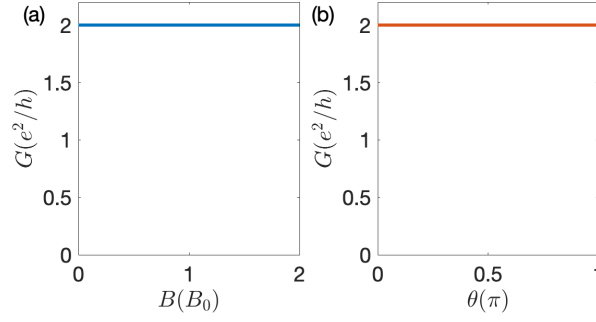


Figure S2. For the two trivial cases 1 (a) and 2 (b) as discussed in this section, the conductance is quantized at $2e^2/h$ and has no dependence on either the field strength B or field direction θ .

- Case 1: the leads are also made of the same SOTIs. Chiral hinge states exist in all regions of space and pass from one lead to the other lead directly;
- Case 2: the leads are made of conventional semiconductors or topological insulators but highly doped. In this case, there are too many channels in the leads such that chiral hinge states lose quantum coherence once entering the leads.

The results for these two cases are presented in Fig. S2. The two-terminal conductance is fixed at $2e^2/h$ and has no dependence on neither the field strength B nor the direction θ .

Appendix S5: Parametrizing the scattering matrix

In this section, we parameterize the scattering matrix with the help of the numerical method. There are two interfaces in our proposed setup. Each interface is described by a 4×4 scattering matrix, i.e., S_L and S_R as listed above, respectively. Due to time-reversal symmetry breaking, S_L and S_R are unitary matrices. Parametrizing these scattering matrices is cumbersome because of the choice of at least 16 free parameters. Instead, we obtain the scattering matrices directly from numerical simulations as explained below.

Let us consider a simpler junction with two semi-infinite regions in z direction: one region is made of a trivial insulators in the region $z < 0$, and the other regions made of the SOTI in the region $z > 0$. The parameters for lead and SOTI are taken the same as those in our interference setup. Then, the interface of this simpler setup mimics the left interface of our interference setup. The scattering matrix at this interface can be obtained numerically by calculating the retarded Green functions for the two regions and then employing the Fisher-Lee relation, or directly using the Kwant algorithm [67]. A similar procedure applies for the right interface.

Known from the conductance, described by Eqs. (2) and (3) in the main text, the relevant four matrices are t_L, t_R, r_L and r_R (or another group t_L, t_R, r_L and $r_{R'}$). Under the same parameter setting with the original setup, we obtain the four matrices as

$$\begin{aligned}
 t_L &= \begin{pmatrix} -0.06198685 + 0.18465009i, & -0.7498761 - 0.16515456i \\ 0.60757993 + 0.469507i, & 0.10194116 - 0.16596995i \end{pmatrix}, \\
 t_R &= \begin{pmatrix} 0.55777311 + 0.34346096i, & -0.0156968 + 0.44520283i \\ -0.26134039 - 0.36076744i, & -0.27139131 + 0.59617366i \end{pmatrix}, \\
 r_L &= \begin{pmatrix} 0.17964098 - 0.37617273i, & 0.39605429 + 0.20453843i \\ 0.25086872 - 0.36845604i, & -0.33709527 - 0.2452419i \end{pmatrix}, \\
 r_R &= \begin{pmatrix} -0.40202362 - 0.44148246i, & -0.06268933 - 0.1095996i \\ 0.05582996 + 0.1132477i, & -0.14131563 - 0.58013761i \end{pmatrix}. \tag{S5.1}
 \end{aligned}$$

Figure S3 presents the transport properties obtained using the analytical formula Eq. (3) in the main text after we parameterize the relevant scattering matrix according to the corresponding parameter settings. We see that the main features of the conductance are qualitatively the same as the numerical results in Fig. 2 of the main text. As shown in Fig. S3 (a), each pattern has single frequency; the oscillation amplitude is larger at $\theta = \pi/4$; and the period of red

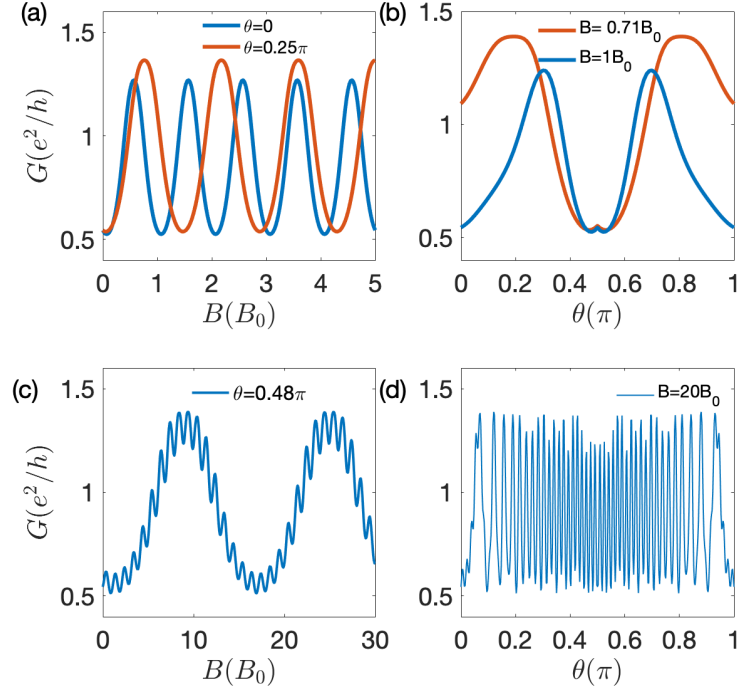


Figure S3. Transport properties obtained using the analytical formula, Eq. (3) in the main text, after we parametrize the relevant scattering matrix according to the corresponding parameter settings. (a) Conductance oscillation pattern as function of field strength B for different field directions $\theta = 0$ and $\theta = 0.25\pi$, respectively. (b) Conductance oscillation pattern as function of field direction θ for different field strengths $B = B_0/\sqrt{2} \approx 0.71B_0$ and $B = 1B_0$, respectively. (c) Beating pattern of conductance as function of field strength B . (d) Beating pattern of conductance as function of field direction θ .

line is about $\sqrt{2}$ times that of the blue line. In Fig. S3 (b), there are two peaks and the oscillation amplitude is more pronounced when $B = B_0/\sqrt{2} \approx 0.71B_0$. In Fig. S3 (c), the conductance shows a beating pattern of B at $\theta = 0.48\pi$. Finally, in Fig. S3 (d), the conductance shows an “irregular” beating pattern as a function of θ for large B .

Appendix S6: Model of \mathcal{C}_6 symmetric SOTIs

The effective model for a \mathcal{C}_6 symmetric SOTI on a stacked hexagonal lattice can be written as [63]

$$H_{\text{hex}} = \begin{pmatrix} h + ms_z\sigma_0 & h_{AB} \\ h_{AB}^\dagger & h + ms_z\sigma_0 \end{pmatrix}, \quad (\text{S6.1})$$

where

$$\begin{aligned} h &= \tilde{C} - \frac{4}{3}C_2(\cos k_1 + \cos k_2 + \cos k_3) + \frac{v}{3}(2\sin k_1 + \sin k_2 + \sin k_3)\Gamma_1 \\ &\quad + \frac{v}{\sqrt{3}}(\sin k_2 - \sin k_3)\Gamma_2 + w[-\sin k_1 + \sin k_2 + \sin k_3]\Gamma_4 + \left[M - \frac{4}{3}M_2(\cos k_1 + \cos k_2 + \cos k_3)\right]\Gamma_5 \\ h_{AB} &= -2C_1 \cos k_z + 2v_z \sin k_z \Gamma_3 - 2M_1 \cos k_z \Gamma_5, \end{aligned} \quad (\text{S6.2})$$

and $k_1 = k_x$, $k_2 = (k_x + \sqrt{3}k_y)/2$ and $k_3 = k_1 - k_2$. h_{AB} describes the hopping between neighboring layers. The Γ matrices are defined as $\Gamma_i = s_i\sigma_1$ with $i \in \{1, 2, 3\}$, $\Gamma_4 = s_0\sigma_2$ and $\Gamma_5 = s_0\sigma_3$ with \mathbf{s} and σ the Pauli matrices and s_0 and σ_0 the corresponding identity matrices. The model parameters are defined as $\tilde{C} = C_0 + 2C_1 + 4C_2$, and $\tilde{M} = M_0 + 2M_1 + 4M_2$. In the numerical calculations, we set the parameters $C_0 = 0$, $C_1 = C_2 = 0.5$, $M_0 = -2.5$, $M_1 = M_2 = 1$, $v = v_z = 1$, $m = 0.5$ and $w = 2$. The perimeter of the hexagonal prisms is $6 \times n_s$ with side length $n_s = 25a$ and $L_z = 50a$.

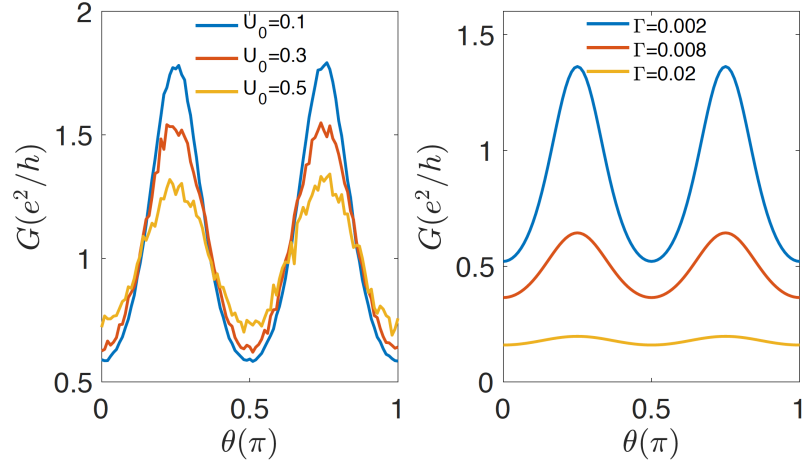


Figure S4. Left panel: influence of disorder on the interference pattern. We average over 100 disorder configurations. Right panel: influence of dephasing on the interference pattern. We choose parameters: $L_z = 60a$, $W_x = W_y = 12a$, $m = 2$, $b = -1$, $v = 1$, $\Delta = 1$. The magnetic field strength is fixed at $B = B_0/\sqrt{2} \approx 0.71B_0$.

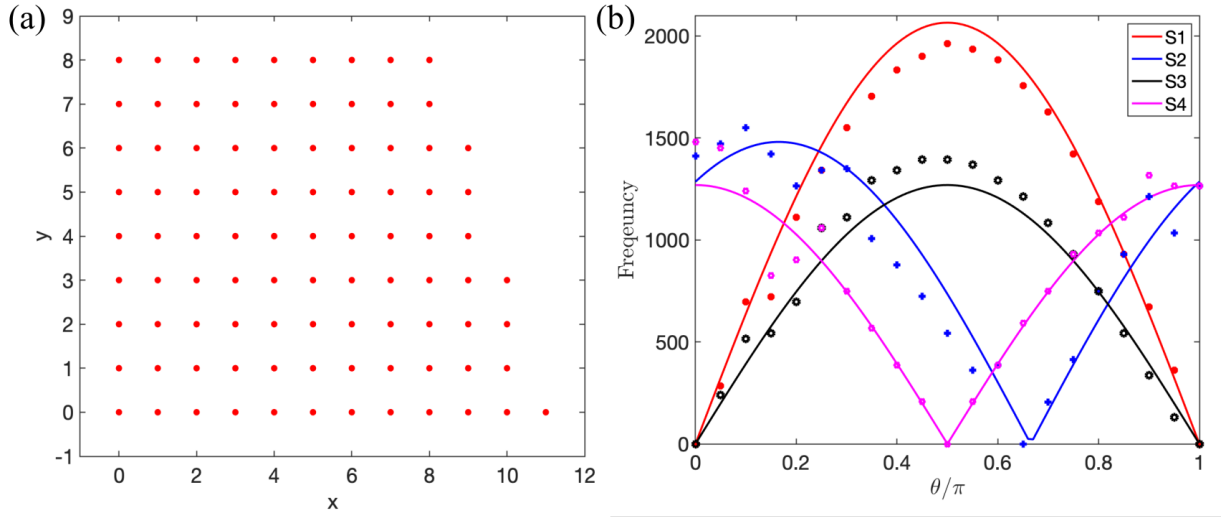


Figure S5. (a) Cross section of the SOTI in a trapezoid geometry. (b) Four frequencies as functions of field direction θ . Here, S1 (S2, S3, S4) indicates the bottom (right-side, top, left-side) surface of the trapezoid. Solid lines are analytical results, and the dotted lines are obtained by Fourier transformation from the conductance beating pattern. Discrepancy between them maybe due to the finite-size effects. We choose parameters for the SOTI as: $L_z = 200a$, $m = 2$, $b = -1$, $v = 1$, and $\Delta = 1$.

Appendix S7: Disorder and dephasing

In this section, we show that the interference pattern of our interferometer is robust against disorder and dephasing.

To mimic disorder, we consider the onsite type $V_{\text{dis}} = V(\mathbf{r})I_{4 \times 4}$ with random function $V(\mathbf{r})$ distributed uniformly within the interval $[-U_0/2, U_0/2]$ and U_0 being the disorder strength. It is shown in Fig. S4 that as increasing the disorder strength U_0 , the oscillation amplitude decreases gradually. However, the interference pattern of the conductance remains even when the disorder strength is quite strong (comparable with the bulk gap).

We also consider dephasing in the SOTI region in our setup by attaching each site in the discretized lattice model with a virtual lead [64]. These virtual leads are coupled to the system via the self-energy $-i\Gamma/2$ with Γ measuring the dephasing strength ($1/\Gamma$ signifies the quasiparticle life time). It is shown in Fig. S4 that the interference pattern of the conductance remains under weak dephasing strength. As increasing dephasing strength Γ , the electrons loose

their phase memory quickly and thus the oscillation amplitudes decrease accordingly.

The above results shows the oscillation pattern basically remains under weak disorder and dephasing, which indicates the robustness of our proposal to show quantum interference of hinge states.

Appendix S8: Multiple frequencies when the cross section is a trapezoid

In this section, we present the multiple-frequency case when the cross section of SOTI is a trapezoid, as shown in Fig. S5(a). In this case, there are generally four frequencies in the conductance oscillation as function of field strength B . Figure S5(b) shows the four frequencies as varying the field direction θ . The numerical results are basically consistent with the analytic ones (obtained by the effective surface areas).

One can see from Fig. S5(b) that the four frequencies do not increase or decrease simultaneously, which stems from the 3D nature of the interferometer, as discussed in the main text. Beside, we find that there always exist two field directions (the field directions along the diagonal of the trapezoid), at which only two of the four frequencies will survive.
